5-1-2018

Vortex Gust Interactions with Oscillating Joukowski Airfoil

Huansheng Chen
Lehigh University, huc216@lehigh.edu

Vortex gust interactions with oscillating Joukowski airfoil

by

Huansheng Chen

A Thesis

Presented to the Graduate and Research Committee

of Lehigh University

in Candidacy for the Degree of

Master of Science

in

Mechanical Engineering and Mechanics

Lehigh University

May 2018

This thesis is accepted and approved in partial fulfillment of the requirements for the Master of Science.

_____
Date

_____
Dr. Justin W. Jaworski, Thesis Advisor

_____
Prof. D. Gary Harlow, Chairperson of
Department of Mechanical Engineering and Mechanics

Acknowledgements

I would like to thank my thesis advisor Dr. Justin W. Jaworski who supervised the completion of my thesis. Without his unfailing support and continuous encouragement, I could not make such great process in my studies of Master's degree, and this accomplishment would not be possible without him.

Contents

List of Figures

Abstract

The dynamic interactions between a line vortex and a Joukowski airfoil in harmonic motion are determined analytically and simulated numerically. The equations of vortex motion and the fluid forces on the airfoil are derived from two-dimensional inviscid potential flow theory for fixed and heaving airfoil configurations, and the continuous shedding of vorticity from the trailing edge is modelled by the emended Brown and Michael equation. Special attention is paid to limiting cases of flat airfoils that are either stationary or under prescribed harmonic motions. This work extends beyond these restrictions to include the effects of airfoil thickness and camber on the incoming vortex path, and the dynamic interplay between the vortical field and the prescribed harmonic motions of the airfoil.

Chapter 1

Introduction

1.1 Motivation

Coherent vortices in the atmosphere or generated by aircraft creates a gust field that can produce unsteady aerodynamic forces on aircraft flying through such a field. For example, in Autonomous Formation Flight (AFF), the streamwise-oriented vortices from the wingtips of the leader aircraft can have a significant influence on the aerodynamics of the follower aircraft, as shown in Fig. 1.1a. For example, in 2001, flight tests of F/A-18s in formation showed that the induced drag reduced due to vortex impingement on the following F/A-18s led to 14% fuel savings of the trailing aircraft compared to the fuel consumption when flying alone [20]. Similar phenomena occurs in migrating bird flight [5], as shown in Fig. 1.1b. As each bird flaps its wings, the vortex wake creates an 'upwash' for the birds downstream. By flying in a 'vee' formation, the flock as a whole achieves a 70% greater flying range than the capacity of an individual bird [5].

The interactions of solid bodies with streamwise vortices or vortex structures with other orientations are reviewed by Rockwell [19]. Of present interest is the spanwise-oriented vortex, whose motion is coupled aeroelastically to transverse deformation of the wings; this scenerio is related to the classical tunnel gust problem that is common to aircraft [19]. Such unsteady vortical gust conditions affect the aerodynamic forces on the wing and produce

(a)  (b) 

Figure 1.1: Examples of vortex-wing interactions: (a) a pair of F/A-18s in Autonomous Formation Flight; (b) geese fly in a "V" formation

an unsteady vortex wake that is also coupled to the motion of the incident vortex and to the wing shape and position. The coupled interactions and effects of the vortex trajectory, airfoil motions and airfoil geometry are examined theoretically in this thesis.

1.2 Background

Two-dimensional high-Reynolds-number flow moving past a thin airfoil is a classical problem in fluid-structure interactions that has received considerable attention in the past decades. A general schematic of the model problem is shown in Fig. 1.2. The schematic directs the mathematical modeling to describe a Joukowski airfoil on elastic supports in a two-dimensional uniform flow that encounters a line vortex Γ and sheds a vortex γ_k, whose strength satisfies the Kutta condition and whose motion obeys the emended Brown and Michael equation [8]. Σ denotes the entire vorticity field, α is the angle of attack, and k_α and k_h are the spring stiffnesses for the system. For the present work, no aeroelastic motions (k_h=0) are considered; however, prescribed harmonic plunging motions are considered in the present work. The general scenario shown in Fig. 1.2 can be pared down to simpler problems for verification purposes, which are outlined in §3.1 and §3.2. The procedures to generalize the formulations to include the Joukowski airfoil shape and its prescribed motions are identified in Chapter 4.

For theoretical analyses in particular, the representation of how vorticity is shed into the

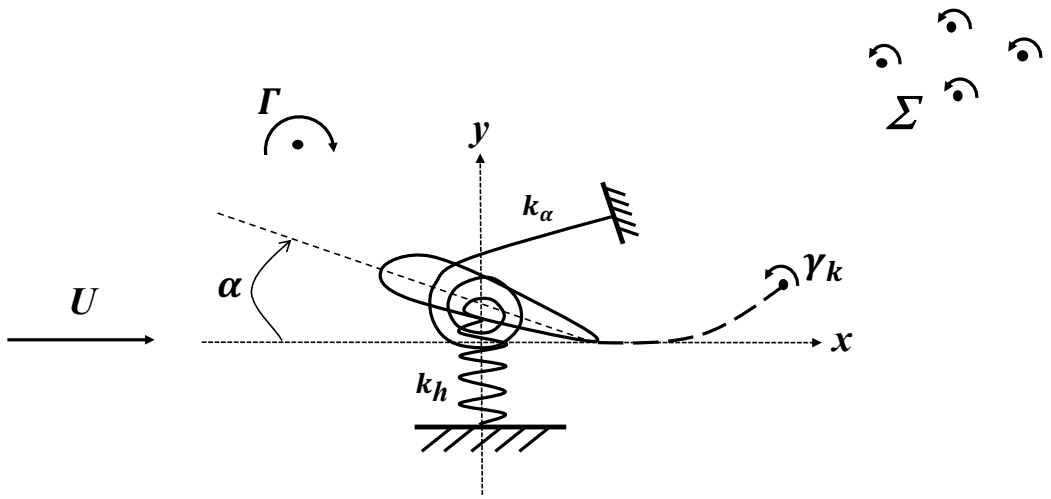

Figure 1.2: Schematic of the generalized model problem of vortex gust interactions with an airfoil on elastic supports. Only fixed and prescribed harmonic plunging airfoil motions are considered in this work.

wake to satisfy the Kutta condition at the trailing edge plays a crucial role in gust-airfoil interactions and their related unsteady airfoil problems. In contrast to continuous-wake models of thin airfoil problems, Brown and Michael [3] developed a wake model involving coherent vortices to model vortex shedding from a delta wing. Their model supposed that the shed vorticity rolls up via a connecting vortex sheet into a point vortex with time-varying circulation, and this model has also formed the basis of many numerical simulations of unsteady vortex shedding. For example, Cortelezzi and Leonard [4] analyzed the two-dimensional unsteady separated flow past a semi-infinite plate with transverse motion. Michelin and Llewellyn Smith [17] described a two-dimensional model for the flapping of an elastic flag immersed in an axial flow, and they later studied the vortex shedding of a heaving flexible wing in a steady flow [16]. Wang and Eldredge [21] developed a point-vortex model for two-dimensional unsteady aerodynamics of a flat plate airfoil.

However, Peters and Hirschberg [18] pointed out that the original Brown and Michael equation does not guarantee the vanishing of a reaction force due to an unbalanced couple, which is of minor concern to the fluid dynamic problem but is important when making acoustic predictions. Howe later corrected this error and put forth the so-called emended Brown and Michael equation [8], in which he compared the wake flow and the acoustic

pressure signature of the original and emended models. Howe concluded that both models exhibit small differences in the predicted wake flow (i.e. the vortex trajectories) near the edge, the predicted acoustic amplitudes (reductions in the radiated sound) for both models are qualitatively the same. However, the predicted noise reduction is smaller for the emended Brown and Michael equation by about 4 dB. The emended Brown and Michael equation has become a popular tool in two-dimensional theoretical approximation of high-Reynolds vortex shedding problems. For example, Howe estimated the sound produced by a line vortex encountering steps [10]. Guo discussed a vortex-airfoil interaction problem to demonstrate the two-dimensional Ffowcs Williams/Hawkings equation [6]. Kuo and Dowling modelled a continuous sound-free vortex shedding of vorticity at a duct exit [13]. Manela and Huang constructed a vortex sound model for a wing-vortex interaction problem involving a movable flap [15]. Manela [14] also studied the combined effects of airfoil motion and of an incident vortex on the sound radiation from a flat plate airfoil, which provides the verification case in the present work for the limit of zero airfoil thickness and camber.

The present work extends beyond the present literature to examine the effects of airfoil thickness and camber together with the dynamically-coupled motions of a coherent incident vortex, airfoil with oscillating motion, and its wake of free vortices. For the theoretical analyses, the gust-airfoil interactions are simplified as the coupling between an incident vortex and a Joukowski airfoil in two spatial dimensions. The present analysis is limited to only heaving motions of the airfoil; pitching is not considered in this analysis. Knowledge of the vortex and airfoil motion enable the prediction of the vortex noise generated by an incident spanwise gust, which is left as an item for future research outside the scope of this thesis and is not pursued here.

1.3 Research questions

This thesis addresses the following research questions:

1. How do the airfoil thickness and camber distributions affect the path of an incident line vortex and induced forces on the airfoil?

2. What is the effect of coupling between the vortex and the airfoil on prescribed harmonic motion?

1.4 Thesis outline

The remainder of the thesis is outlined as follows. A review of the pertinent mathematical background and the technical approach are introduced in Chapter 2. Chapter 3 validates the present mathematical framework against previous work for flat plate airfoils in different scenarios, including the starting vortex problem and the case of multiple shed vortices. The main analysis of gust-airfoil interactions for the Joukowski airfoil is established in Chapter 4. Chapter 5 presents numerical results to verify for theoretical analyses in the former chapters. Chapter 6 summarizes the conclusions and contributions of this work. A pair of appendices are provided at the end of the thesis, which included detailed derivations of the emended Brown and Michael equation in different mathematical formulations.

Chapter 2

Mathematical modelling preliminaries

2.1 Conformal mapping

Conformal mapping provides a general mathematical framework to solve Laplace's equation in a geometrically simple domain and relate the solution back to the original physical domain in two-dimensional potential flows. Suppose a complex function $\zeta = f(z)$ that defines a transformation between points $z = x+iy$ in the z plane and points $\zeta \equiv \xi+i\eta$ in the ζ plane, as shown in Fig. 2.1. A complex potential $w(z) = \phi(x, y) + i\psi(x, y)$ may then be de-

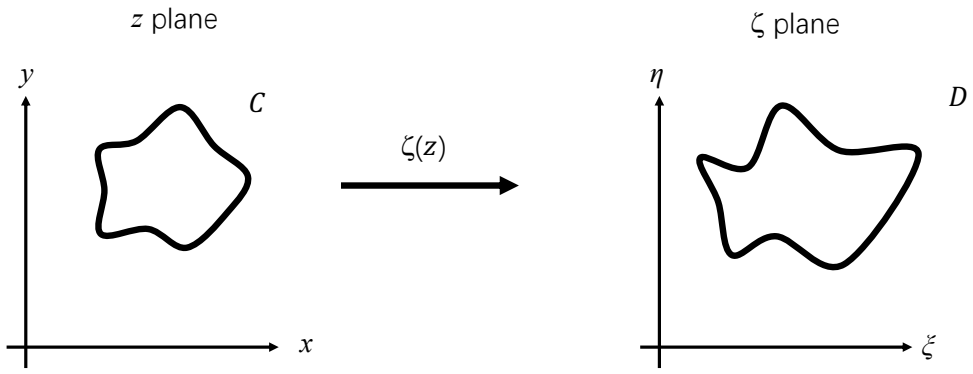

Figure 2.1: Schematic of conformal mapping

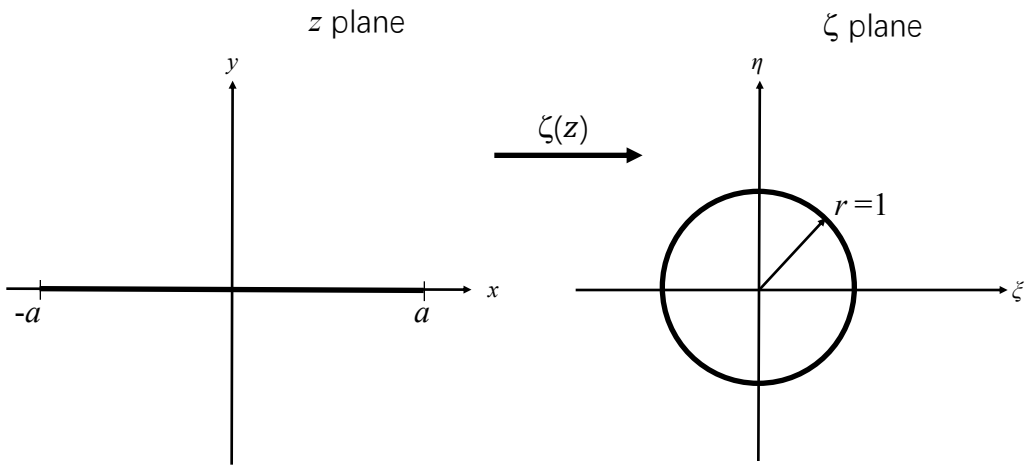

Figure 2.2: Mapping of a flat plate in the physical z-plane to a unit circle in the ζ-plane.

termined, where scalar functions ϕ and ψ both satisfy Laplace's equation [9]. The mapping $\zeta = f(z)$ when $f(z)$ is an analytic function will possible isolate non-analytic points, defines a conformal mapping from a regular region C in the z plane into a region D in ζ plane, where the corresponding functions are Φ and Ψ. It is well known [9] that the solutions Φ and Ψ of Laplace equation in D are the solutions of Laplace's equation in C. Therefore, a conformal transformation allows the flow past a system of rigid boundaries in the z plane to be represented by an equaivalent flow in the ζ plane. Point vortex singularities mapped between the z and ζ planes have the same circulation value in each plane.

2.1.1 Flat plate airfoil

The conformal mapping of the flat plate airfoil in the physical z-plane and the mapped ζ-plane is described by

$$\zeta(z) = \frac{1}{a}(z + \sqrt{z^2 - a^2}). \tag{2.1}$$

Using (2.1), the airfoil is mapped from a stationary flat plate airfoil ($-a \leq z \leq a$, Im$z = 0$) in the physical z-plane ($z = x + iy$) into a circle in ζ-plane ($\zeta = \xi + i\eta$) with a radius $r = 1$ (see Fig. 2.2).

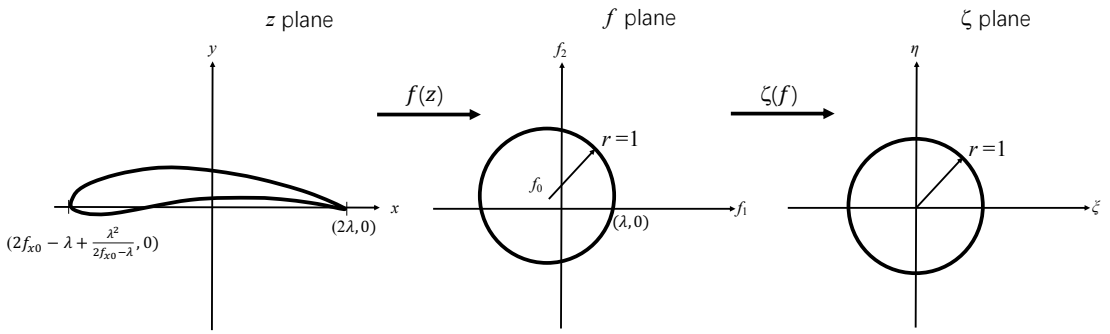

Figure 2.3: Successive mappings of a Joukowski airfoil in the physical z-plane to a unit circle centered at the origin in the ζ-plane.

2.1.2 Joukowski airfoil

From previous introduction of mapping in §2.1, the conformal mapping of the Joukowski airfoil in the physical z-plane and the mapped ζ-plane is described by

$$\zeta(z) = \frac{1}{2}(z + \sqrt{z^2 - 4\lambda^2}) - f_0. \tag{2.2}$$

Using equation (2.2), the Joukowski airfoil in the physical z-plane ($z = x + iy$) with its trailing edge locating at $(2\lambda, 0)$ is mapped in a circle f-plane ($f = f_1 + if_2$) with a radius $r = 1$ (see Fig. 2.3). Note that the offset of the circle center at $f_0 = f_{x0} + if_{y0}$ and the corresponding trailing edge at $(\lambda, 0)$. The circle in f-plane is then mapped into the same unit circle with its origin at $(0, 0)$ in ζ-plane ($\zeta = \xi + i\eta$), and the corresponding trailing edge is at $\lambda - f_0$.

2.2 Equation of vortex motion

2.2.1 Free vortex motion

The equations of motion for a line vortex are derived here and followed the presentation by Howe [9]

$$w'(z_0) = \frac{dz_0^*}{dt}, \tag{2.3}$$

where

$$w_0(z) = w(z) + \frac{i\Gamma}{2\pi}\log\left(z - z_0\right), \tag{2.4}$$

and the asterisk denotes the complex conjugate of a complex number.

Following the conformal mapping introduction in §2.1, and if $\zeta = \zeta(z_0)$ is the image of the line vortex in the ζ plane, the complex potential $w(z)$ may be written in the form

$$w(z) = -\frac{i\Gamma}{2\pi}\log\left(\zeta(z) - \zeta(z_0)\right) + F(z), \tag{2.5}$$

where $\zeta(z)$ and $F(z)$ are regular functions of z in the neighborhood of the line vortex with strength Γ at $z = z_0$. In particular, when $|z - z_0|$ is small, $\zeta(z)$ could be expanded by Taylor series in the form

$$\zeta(z) = \zeta(z_0) + (z - z_0)\zeta'(z_0) + \frac{(z - z_0)^2}{2}\zeta''(z_0) + \cdots +, \tag{2.6}$$

where the primes denote differentiation with respect to z. Therefore, in the neighborhood of the vortex, the complex potential is accomplished by

$$\begin{aligned} w_0(z) &= w(z) + \frac{i\Gamma}{2\pi}\log\left(\zeta(z) - \zeta(z_0)\right), \\ &= -\frac{i\Gamma}{2\pi}\log\left(\zeta(z) - \zeta(z_0)\right) + F(z), \\ &\approx -\frac{i\Gamma}{2\pi}\log\left[\zeta'(z_0) + \frac{1}{2}\zeta''(z_0)(z - z_0)\right] + F(z). \end{aligned} \tag{2.7}$$

Therefore, by substitution of (2.7) into (2.3) and subsequent differentiation, the equation

of the free vortex motion becomes

$$\frac{dz_0^*}{dt} = \frac{dx_0}{dt} - i\frac{dy_0}{dt} = -\frac{i\Gamma\zeta''(z_0)}{4\pi\zeta'(z_0)} + F'(z_0). \tag{2.8}$$

The complex-valued (2.8) equation supplies two nonlinear first-order ODEs for the vortex position (x_0, y_0).

2.2.2 Emended Brown and Michael equation

From the literature [8], it is known that the emended Brown and Michael equation is a reappraisal of original Brown and Michael equation, which is the theoretical basis of approximations of vortex shedding from two-dimensional airfoils in flow with high-Reynolds and low-Mach numbers. A correction is introduced in the emended Brown and Michael equation to account for inconsistent reaction forces introduced by the original Brown and Michael formulation.

The emended Brown and Michael equation is usually represented in vector form

$$\frac{d\boldsymbol{x}_{\gamma_n}}{dt} \cdot \boldsymbol{\nabla}\Psi_i + \frac{\Psi_i}{\gamma_n}\frac{d\gamma_n}{dt} = \boldsymbol{v}_{\gamma_n} \cdot \boldsymbol{\nabla}\Psi_i, \qquad i = 1, 2 \tag{2.9}$$

where $\boldsymbol{x}_{\gamma_n}$ represents the location of a shed vortex tethered to the trailing edge with circulation γ_n in a vector form with respect to the rectangular coordinate system $\boldsymbol{x} \equiv (x, y)$. $\Psi_i(\boldsymbol{x}, t)$ denotes the stream function of complex potential of the flow in the i-direction, and $\boldsymbol{v}_{\gamma_n}$ is the fluid velocity when the local velocity induced by γ_n is excluded.Equation (2.9) can be rearranged into the form

$$\frac{dz_{\gamma_n}^*}{dt} + (H_1 - iH_2)\frac{1}{\gamma_n}\frac{d\gamma_n}{dt} = v_{\gamma_n}^*, \tag{2.10}$$

where $z_{\gamma_n}^* = x - iy$, and $v_{\gamma_n}^* = v_x - iv_y$. Here,

$$v_{\gamma_n}^* = -\frac{i\gamma_n\zeta''(z_{\gamma_n})}{4\pi\zeta'(z_{\gamma_n})} + F'_{\gamma_n}(z_{\gamma_n}). \tag{2.11}$$

Equation (2.10) is the general scalar form of the emended Brown and Michael equation, which will be employed for the theoretical analyses in this work. Specific details related to the derivation of (2.10) can be found in Appendix A.

2.3 Kutta condition

Experimental evidence [12] demonstrates that, when a body with a sharp trailing edge passes through a fluid, the action of the fluid viscosity causes the flow over the upper and lower surfaces to merge smoothly at the trailing edge. As a result, at the trailing edge the pressure is continuous, i.e.there is no pressure jump. This condition, termed the Kutta condition, sets the airfoil circulation to be of sufficient strength to hold the rear stagnation point at the trailing edge. In the present work, the Kutta condition sets the instantaneous circulation γ_n of the vortex shed and tethered to the trailing edge, whose motion is governed by the Brown and Michael equation 2.9.

Chapter 3

Flat plate airfoil problem

3.1 Starting vortex problem

3.1.1 Mathematical model

Consider the degenerate case of a Joukowski airfoil as a rigid flat plate airfoil of length $2a$, which is at a fixed angle of attack α relative to a uniform flow U (see Fig. 3.1). To satisfy the Kutta condition at the sharp trailing edge, a point vortex of time varying circulation $\gamma(t)$ is assumed to be released from the trailing edge only if $d\gamma/dt$ changes sign. The shed vorticity does not change sign in this problem; therefore, the emended Brown and Michael equation is expected to recover the classical, steady thin-airfoil result for large time.

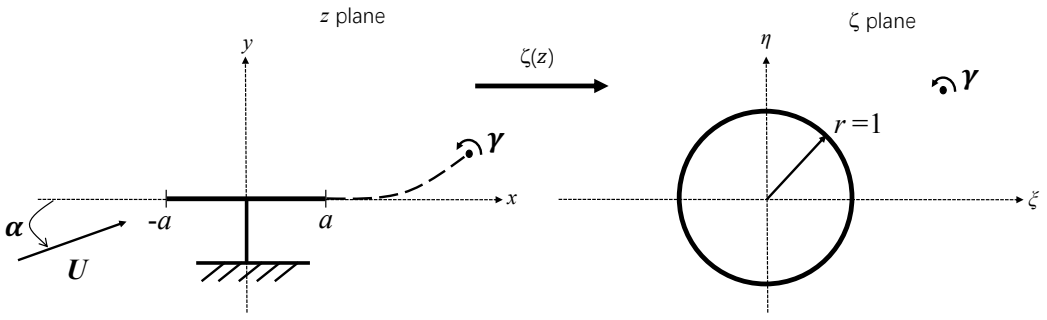

Figure 3.1: Schematic and mapping of starting vortex problem

3.1.2 Flow complex potential

The complex potential of the flow is constructed by superimposing the complex potential to the shed vortex w_γ with that of a uniform flow at angle α,

$$w(\zeta) = w_\gamma + \frac{a}{2}U\left(\zeta e^{-i\alpha} + \frac{1}{\zeta e^{-i\alpha}}\right). \tag{3.1}$$

The complex potential associated with the single shed vortex at ζ_γ in the ζ-plane is

$$w_\gamma(\zeta) = -\frac{i\gamma}{2\pi}\log(\zeta - \zeta_\gamma) + \frac{\mathrm{i}\gamma}{2\pi}\log\left(\zeta - \frac{1}{\zeta_\gamma^*}\right), \tag{3.2}$$

where γ is the time-varying circulation of the shedding vortex, and the complex potential is obtained by placing an image vortex with circulation $-\gamma$ at the inverse point $\zeta = \frac{1}{\zeta_\gamma^*}$ (an asterisk denotes the complex conjugate of a complex number).

Thus, the complex velocity in the mapped ζ-plane is obtained

$$w'(\zeta) \equiv \frac{dw}{d\zeta} = -\frac{i\gamma}{2\pi}\frac{1}{\zeta - \zeta_\gamma} + \frac{i\gamma}{2\pi}\frac{1}{\zeta - \frac{1}{\zeta_\gamma^*}} + \frac{a}{2}U\left(e^{-i\alpha} - \frac{1}{\zeta^2 e^{i\alpha}}\right). \tag{3.3}$$

3.1.3 Evolution of vortex shedding

The motion of the starting vortex is determined by the scalar form of the emended Brown and Michael equation (2.10). For the present case of a flat stationary airfoil with an angle of attack α in the ζ-plane [7],

$$\Psi_1 = \mathrm{Im}\left\{\frac{a}{2}\left(\zeta e^{-i\alpha} + \frac{1}{\zeta e^{-i\alpha}}\right)\right\} \quad \text{and} \quad \Psi_2 = \mathrm{Im}\left\{-i\frac{a}{2}\left(\zeta e^{-i\alpha} - \frac{1}{\zeta e^{-i\alpha}}\right)\right\}. \tag{3.4}$$

Therefore, the corresponding equations of the vortex motion $z_\gamma = x_\gamma + iy_\gamma$ are found by substituting (3.4) into (2.10).

The instantaneous circulation of the vortex $\gamma(t)$ can be determined by applying the

Kutta condition, which requires that the flow velocity at the trailing edge ($\zeta = 1$) vanishes:

$$\gamma(t) = 2\pi a U \sin\alpha \, \frac{|\zeta_\gamma|^2 - 1}{|\zeta_\gamma - 1|^2}. \tag{3.5}$$

3.1.4 Formulation of the dynamical problem

From the introduction of equation of the vortex motion in §2.2, the complex velocity of the starting vortex at z_γ is

$$v_\gamma^* \equiv \frac{dz_\gamma^*}{dt} = -\frac{i\gamma\zeta''(z_\gamma)}{4\pi\zeta'(z_\gamma)} + F'(z_\gamma), \tag{3.6}$$

with

$$F'(z_\gamma) = \frac{a}{2}\left(e^{-i\alpha} - \frac{1}{\zeta_\gamma^2 e^{-i\alpha}}\right)\zeta_\gamma' + \frac{i\gamma}{2\pi}\frac{\zeta_\gamma'}{\zeta - \frac{1}{\zeta_\gamma^*}}. \tag{3.7}$$

Summarizing the above discussion, a system of equations is derived. The real and imaginary parts of the system supply two nonlinear first-order ordinary differential equations for the position $(x_\gamma(t), y_\gamma(t))$ of the starting vortex at time instant t. Here the system of equations is solved numerically using ODE45 in MATLAB. Once the circulation profile of vortex is known, the section lift coefficient of the airfoil C_l can be determined from

$$C_l = \frac{L}{\frac{1}{2}\rho U^2 S} = \frac{\rho U \gamma(t)}{\frac{1}{2}\rho U^2 (2a)} = \frac{\gamma(t)}{Ua} \tag{3.8}$$

The resulting vortex trajectory and time-varying strength can then be determined, and the lift coefficient history can then be compared against existing data for validation. Specific results are shown in §5.1.

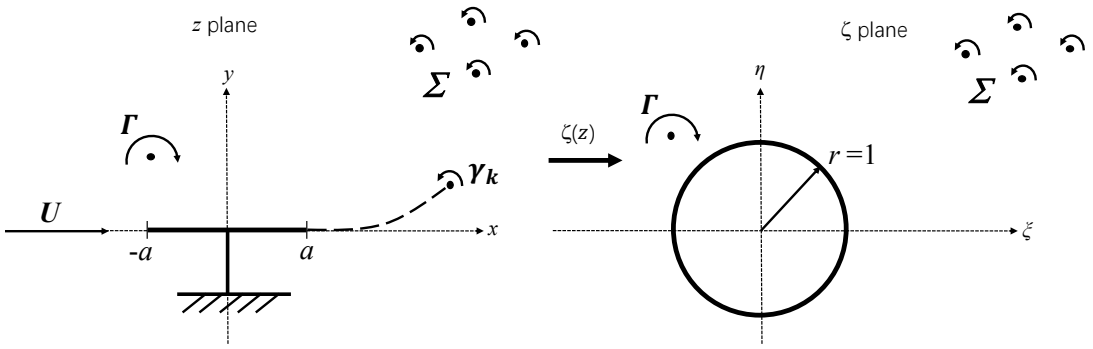

Figure 3.2: Schematic and mapping of multiple vortices problem

3.2 Multiple shedding vortices problem

3.2.1 Mathematical model

Consider a rigid flat plate airfoil of length $2a$ immersed in a uniform flow U in the x-direction. An incident line vortex of constant strength Γ is released into the flow at the initial instant in time ($t = 0$) and pass along the airfoil nearby (see Fig. 3.2). The unsteady forces due to the incident vortex on the airfoil require vorticity to be shed into the wake to satisfy Kelvin's theorem. In this problem, a field of multiple vortices shedding are described by as a set of line vortices whose positions $z_{\gamma_n} = x_{\gamma_n} + iy_{\gamma_n}$ $(n = 1, 2, 3, \cdots)$ and strengths γ_n $(n = 1, 2, 3, \cdots)$ change with time. The position and strength of a vortex tethered to the trailing edge is governed by the emended Brown and Michael equation. If $d\gamma_n/dt$ of the tethered vortex changes sign, the strength of the vortex becomes fixed and the vortex is released from the trailing edge, i.e. moves as a free vortex. This scenario has been previously investigated by Manela [14] and furnishes a verification case for the more general framework in Chapter 4.

3.2.2 Flow complex potential

The conformal mapping for this scenario is the same as in §3.1.1 for the flat plate airfoil. However, the complex potential of the flow changes due to the introduction of an incident

line vortex. The complex potential of the flow becomes:

$$w(\zeta) = w_\gamma + w_\Gamma + \frac{a}{2}U\left(\zeta + \frac{1}{\zeta}\right), \tag{3.9}$$

in which w_Γ is determined by placing an image vortex with circulation $-\Gamma$ at the inverse point $\zeta_\Gamma = 1/\zeta_\Gamma^*$, together with a vortex Γ at the center of the unit circle. The two interior vortices ensure that the total circulation around the circle vanishes. Then

$$w_\Gamma(\zeta) = -\frac{i\Gamma}{2\pi}\log\left(\zeta - \zeta_\Gamma\right) + \frac{\mathrm{i}\Gamma}{2\pi}\log\left(\zeta - \frac{1}{\zeta_\Gamma^*}\right) - \frac{\mathrm{i}\Gamma}{2\pi}\log\,\zeta. \tag{3.10}$$

Now the complex potential of the shedding vortices is given by the sum

$$w_\gamma(\zeta) = \sum_{k=1}^{n}\left(-\frac{i\gamma_k}{2\pi}\log(\zeta - \zeta_{\gamma_\mathrm{k}}) + \frac{\mathrm{i}\gamma_\mathrm{k}}{2\pi}\log\left(\zeta - \frac{1}{\zeta_{\gamma_\mathrm{k}}^*}\right)\right), \tag{3.11}$$

where γ_k is the circulations of $n-1$ free vortices composing the trailing edge wake, which have been released from the trailing edge when $d\gamma_k/dt$ $(k = 1, 2, ..., n-1)$ changed sign.

3.2.3 Evolution of vortex shedding

The motion of the most-recently shed vortices is determined by the scalar form of the emended Brown and Michael equation derived in §2.4. To better understand the complex form of the emended Brown and Michael equation derived by Manela [14], it is instructive to start with the developing of original form of the emended Brown and Michael equation (2.9) and derived the scalar form (2.10). For the present case of a thin stationary airfoil at zero angle of attack in the z-plane [11],

$$\Psi_1 = \mathrm{Im}\left\{z\right\} \quad \text{and} \quad \Psi_2 = \mathrm{Im}\left\{-i\sqrt{z^2 - a^2}\right\}. \tag{3.12}$$

Therefore, the corresponding equations of the vortex motion $z_{\gamma_n} = x_{\gamma_n} + iy_{\gamma_n}$ is found by substituting (3.12) into (2.10):

$$\frac{dz^*_{\gamma_n}}{dt} + \left(\frac{\mathrm{Im}\left\{-i\sqrt{z^2_{\gamma_n} - a^2}\right\} - y\mathrm{Im}\left\{\frac{z_{\gamma_n}}{\sqrt{z^2_{\gamma_n}-a^2}}\right\}}{\mathrm{Im}\left\{-i\frac{z_{\gamma_n}}{\sqrt{z^2_{\gamma_n}-a^2}}\right\}} - iy \right) \frac{1}{\gamma_n}\frac{d\gamma_n}{dt} = v^*_{\gamma_n}. \tag{3.13}$$

It is proved in subsequent numerical results in Chapter 5 that (3.13) is equivalent to the complex form of the emended Brown and Michael equation derived by Manela in his paper [14]. The detailed derivation procedure is presented in Appendix B.

Similarly, the instantaneous circulation of the vortex $\gamma_n(t)$ is obtained

$$\gamma_n(t) = \frac{|\zeta_{\gamma_n} - 1|^2}{|\zeta_{\gamma_n}|^2 - 1}\left(\frac{2\Gamma(1 - \mathrm{Re}\{\zeta_\Gamma\})}{|\zeta_\Gamma - 1|^2} - \sum_{k=1}^{n-1} \gamma_k \frac{|\zeta_{\gamma_k}|^2 - 1}{|\zeta_{\gamma_k} - 1|^2} \right). \tag{3.14}$$

3.2.4 Formulation of the problem

From the equations of vortex motion introduced in §2.2, the position of the incident line vortex z_Γ obeys

$$\frac{dz^*_\Gamma}{dt} = -\frac{i\Gamma\zeta''(z_\Gamma)}{4\pi\zeta'(z_\Gamma)} + F'(z_\Gamma), \tag{3.15}$$

with

$$F'_\Gamma(z_\Gamma) = \frac{i\Gamma}{2\pi}\frac{\zeta'_\Gamma}{(\zeta^2_\Gamma - 1)\zeta_\Gamma} - \frac{i\zeta'_\Gamma}{2\pi}\sum_{k=1}^{n} \gamma_k \left(\frac{1}{\zeta_\Gamma - \zeta_{\gamma_k}} - \frac{1}{\zeta_\Gamma - 1/\zeta^*_{\gamma_k}} \right) + 1. \tag{3.16}$$

Note that equation (3.16) corrects a typographical error in the first term of $F'(z_\Gamma)$ in Manela [14].

Similarly, the equation of motion for the $n-1$ free vortices is

$$\frac{dz^*_{\gamma_k}}{dt} = -\frac{i\gamma_k\zeta''(z_{\gamma_k})}{4\pi\zeta'(z_{\gamma_k})} + F'_{\gamma_k}(z_{\gamma_k}), \tag{3.17}$$

with

$$F'_{\gamma_k}(z_{\gamma_k}) = \frac{i\Gamma}{2\pi}\zeta'_{\gamma_k}\left(\frac{1}{\zeta_{\gamma_k}-\zeta_\Gamma} - \frac{1}{\zeta_{\gamma_k}-1/\zeta^*_\Gamma} + \frac{1}{\zeta_{\gamma_k}}\right) + \frac{i\gamma_k}{2\pi}\frac{\zeta'_{\gamma_k}}{\zeta_{\gamma_k}-1/\zeta^*_{\gamma_k}}$$
$$-\frac{i\zeta'_{\gamma_k}}{2\pi}\sum_{m=1,m\neq k}^{n}\gamma_m\left(\frac{1}{\zeta_{\Gamma_k}-\zeta_{\gamma_m}} - \frac{1}{\zeta_{\gamma_k}-1/\zeta^*_{\gamma_m}}\right) + 1. \tag{3.18}$$

The equation of motion for the shedding vortex is also determined by (3.17) and (3.18) with $k = n$.

The system of equations is formed by combining equations (3.15) to (3.18), which consists of $2(n+1)$ first-order ordinary differential equations for the position $(x_\Gamma(t), y_\Gamma(t))$ of the incident vortex and the positions $(x_{\gamma_n}(t), y_{\gamma_n}(t))$ of n trailing edge vortices. The system of equations is solved numerically using ODE45 in MATLAB, and results are compared in § 5.2 with the results that Manela obtained in his paper [14].

Chapter 4

Joukowski airfoil problem

4.1 Mathematical model

Now consider a general case of a Joukowski airfoil subject to a parallel uniform flow U in the x-direction. An incident line vortex of constant strength Γ is released into the flow at the initial instant in time ($t = 0$) and passes near the Joukowski airfoil (see Fig. 4.1). And the airfoil moves harmonically in the y-direction with prescribed heaving motion

$$h(t) = 2\varepsilon\lambda\cos(\omega t), \qquad t \geq 0, \tag{4.1}$$

where $\varepsilon \ll 1$ and ω is the frequency of the heaving motion. Vortex shedding is produced to satisfy the Kutta condition at the trailing edge of the airfoil. In this problem, we consider

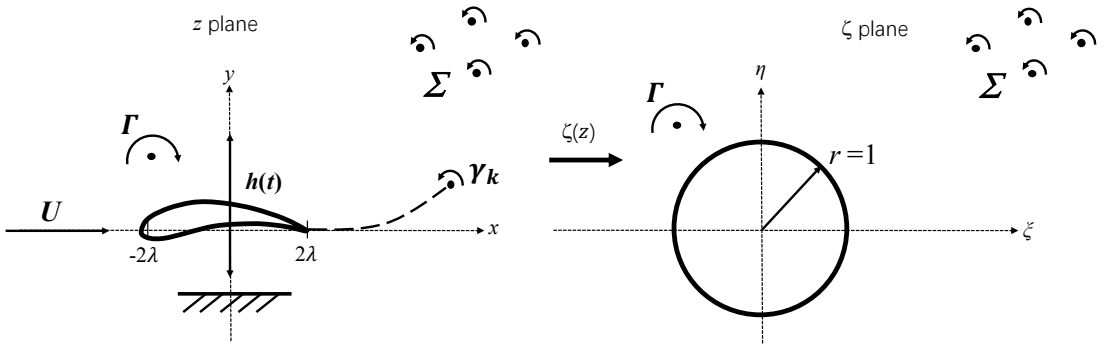

Figure 4.1: Schematic of Joukowski airfoil problem

multiple vortices shedding which is discretized as a set of line vortices whose position $z_{\gamma_n} = x_{\gamma_n} + iy_{\gamma_n}$ $(n = 1, 2, 3, \cdots)$ and strength γ_n $(n = 1, 2, 3, \cdots)$ change with time. Only if $d\gamma_n/dt$ changes sign will a tethered vortex obeying the Brown and Michael equation be released and allowed to move as a free vortex.

4.2 Flow complex potential

The complex potential of the flow is similar to that in §3.2.2 and as follows

$$w(\zeta) = w_\gamma + w_\Gamma + w_h + U\left(\zeta + f_0 + \frac{\lambda^2}{\zeta + f_0}\right). \tag{4.2}$$

The complex potentials $w_\Gamma(\zeta)$, $w_\gamma(\zeta)$ and $w_h(\zeta)$ are obtained by using mapping transformation introduced in (2.2). With time-dependent airfoil vortices considered, (2.2) becomes

$$\zeta(s) = \frac{1}{2}\left[s(z,t) + \sqrt{s^2 - 4\lambda^2}\right] - f_0, \qquad s(z,t) = z - ih(t). \tag{4.3}$$

Using (4.3), the Joukowski airfoil under prescribed heaving motion in z-plane is mapped into a stationary airfoil in s-plane. This mapping yields

$$w_\Gamma(\zeta) = -\frac{i\Gamma}{2\pi}\log\left(\zeta - \zeta_\Gamma\right) + \frac{\mathrm{i}\Gamma}{2\pi}\log\left(\zeta - \frac{1}{\zeta_\Gamma^*}\right) - \frac{\mathrm{i}\Gamma}{2\pi}\log\zeta, \tag{4.4}$$

$$w_\gamma(\zeta) = \sum_{k=1}^{n}\left(-\frac{i\gamma_k}{2\pi}\log\left(\zeta - \zeta_{\gamma_k}\right) + \frac{i\gamma_k}{2\pi}\log\left(\zeta - \frac{1}{\zeta_{\gamma_k}^*}\right)\right), \tag{4.5}$$

$$w_h(\zeta) = iV\left(\zeta - \frac{1}{\zeta}\right), \tag{4.6}$$

where $V = dh/dt$ is the vertical velocity of the harmonic motion of the Joukowski airfoil [1].

4.3 Evolution of vortex shedding

The motions of the shed vortices are determined by the scalar form of the emended Brown and Michael equation (2.10), For a Joukowski airfoil in the ζ-plane [7]

$$\Psi_1 = \mathrm{Im}\left\{\zeta + \frac{1}{\zeta}\right\} \quad \text{and} \quad \Psi_2 = \mathrm{Im}\left\{-i(\zeta - \frac{1}{\zeta})\right\}. \tag{4.7}$$

Using (2.10) and (4.7), the corresponding equations of the vortices motion are established.

Similarly, the instantaneous circulation of the vortex $\gamma_n(t)$ is obtained

$$\gamma_n(t) = \frac{|T^*\zeta_{\gamma_n} - 1|^2}{|\zeta_{\gamma_n}|^2 - 1}\left(\frac{2\Gamma\left(1 - \mathrm{Re}\{T^*\zeta_\Gamma\}\right)}{|T^*\zeta_\Gamma - 1|^2} - \sum_{k=1}^{n-1}\gamma_k\frac{|\zeta_{\gamma_k}|^2 - 1}{|T^*\zeta_{\gamma_k} - 1|^2} - 2\pi V\mathrm{Re}\left(T^*\right)\right), \tag{4.8}$$

in which T^* is complex conjugate of the trailing edge T location ($T = \lambda - f_0$) in the ζ-plane.

4.4 Formulation of the dynamical problem

The complex velocity of the incident line vortex at s_Γ is

$$\frac{ds_\Gamma^*}{dt} = -\frac{i\Gamma\zeta''(s_\Gamma)}{4\pi\zeta'(s_\Gamma)} + F'(s_\Gamma), \tag{4.9}$$

where

$$F'_\Gamma(s_\Gamma) = \frac{i\Gamma}{2\pi}\frac{\zeta'_\Gamma}{(\zeta_\Gamma^2 - 1)\zeta_\Gamma} - \frac{i\zeta'_\Gamma}{2\pi}\sum_{k=1}^{n}\gamma_k\left(\frac{1}{\zeta_\Gamma - \zeta_{\gamma_k}} - \frac{1}{\zeta_\Gamma - 1/\zeta^*_{\gamma_k}}\right) + iV\zeta'_\Gamma\left(1 + \frac{1}{\zeta_\Gamma^2}\right) + U \tag{4.10}$$

Similarly, the equations of motion for the $n-1$ free vortices are determined

$$\frac{ds^*_{\gamma_k}}{dt} = -\frac{i\gamma_k\zeta''(s_{\gamma_k})}{4\pi\zeta'(s_{\gamma_k})} + F'_{\gamma_k}(s_{\gamma_k}), \tag{4.11}$$

where

$$F'_{\gamma_k}(s_{\gamma_k}) = \frac{i\Gamma}{2\pi}\zeta'_{\gamma_k}\left(\frac{1}{\zeta_{\gamma_k}-\zeta_\Gamma} - \frac{1}{\zeta_{\gamma_k}-1/\zeta^*_\Gamma} + \frac{1}{\zeta_{\gamma_k}}\right) + \frac{i\gamma_k}{2\pi}\frac{\zeta'_{\gamma_k}}{\zeta_{\gamma_k}-1/\zeta^*_{\gamma_k}}$$
$$-\frac{i\zeta'_{\gamma_k}}{2\pi}\sum_{m=1,m\neq k}^{n}\gamma_m\left(\frac{1}{\zeta_{\Gamma_k}-\zeta_{\gamma_m}} - \frac{1}{\zeta_{\gamma_k}-1/\zeta^*_{\gamma_m}}\right) + iV\zeta'_{\gamma_k}\left(1+\frac{1}{\zeta^2_{\gamma_k}}\right) + 1. \tag{4.12}$$

The system of dynamical equations is formed from equations (4.9) to (4.12), which consists of $2(n+1)$ first-order ordinary differential equations for the position $(s_{x_\Gamma(t)}, s_{y_\Gamma(t)})$ of the incident vortex and the positions $(s_{x_{\gamma_n}(t)}, s_{y_{\gamma_n}(t)})$ of n trailing edge vortices. The system of equations is also solved numerically using ODE45 in MATLAB. Once solved, the results are mapped into the z-plane by using $z(t) = s(t) + ih(t)$.

Chapter 5

Results and Analysis

This chapter presents and describes the numerical simulation based upon the theoretical analyses of the previous chapters. These results are separated into four main sections: (1) a discussion of the verification of results in the starting vortex problem, where the results are compared with the classical Küssner function approximation; (2) an examination of the results of Manela [14], which involves multiple vortices shedding from a fixed flat plate airfoil; (3) the results of an upgraded version of (2) when airfoil thickness and camber are considered in the case of a Joukowski airfoil; (4) the results of an extended version of section (3) when the Joukowski airfoil is under prescribed harmonic motion.

5.1 Starting shedding vortex

The mathematical problem is rendered dimensionless using the length, velocity and time scales of a, U, a/U. Dimensionless quantities are marked by overbars. For starting vortex problem, the initial trailing edge location is specified to be $\overline{z}_\gamma(0) = z_\gamma(0)/a = (1, 0.0001)$, and the angle of attack is set arbitrarily to $\alpha = 10°$. Figure 5.1 compares the path of the starting vortex with respect to $\bar{t}$ with an asymptote with a slope of $10°$. The resulting lift coefficient on the airfoil calculated from Kelvin's theorem is also compared, where the numerical results of C_L/α agree with the classical Padé approximant of the

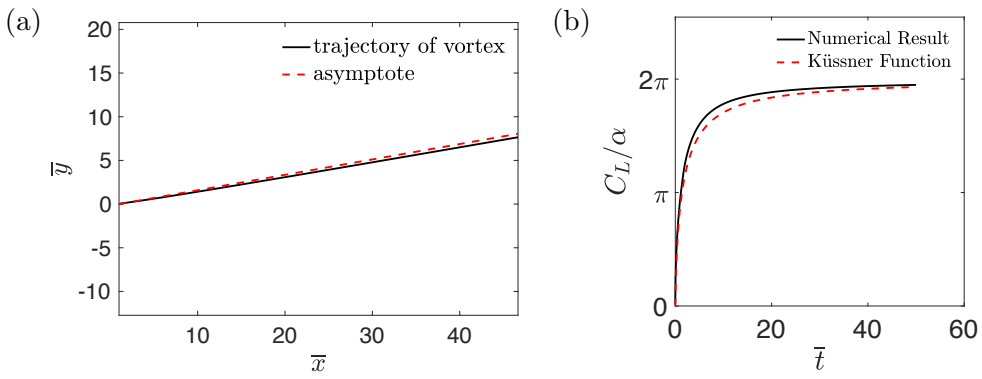

Figure 5.1: Starting vortex trajectory and lift history: (a) the trajectory of the starting vortex starts from the trailing edge and the asymptote with a slope of 10°; (b) time history comparison of C_L/α between the numerical results and the Küssner function approximation.

Küssner function [2]

$$K(t) = 2\pi \frac{\left(\bar{t}^2 + \bar{t}\right)}{\left(\bar{t}^2 + 2.82\bar{t} + 0.80\right)}. \tag{5.1}$$

5.2 Multiple shedding vortices

The setup of the non-dimensional method and initial conditions replicate those by Manela [14] to furnish a direct comparison: $\overline{x} = x/a$, $\overline{y} = y/a$ and $\overline{\Gamma} = \Gamma/(2\pi U a)$, and the initial line-vortex location is $\overline{z}_\Gamma(0) = z_\Gamma(0)/a = (-20, 0.2)$. Setting the initial shed vortex location to be $\overline{z}_\gamma(0) = z_\gamma(0)/a = (1, 0.0001)$. It was found from the results that after the third vortex is shed from the trailing edge, $d\gamma_3/dt$ did not change sign any more. Therefore, the trailing edge wake can be described by shedding only three vortices in maximum. Results including the trajectories of three shed vortices and strengths are illustrated in Figure 5.2, which are in agreement with Manela [14].

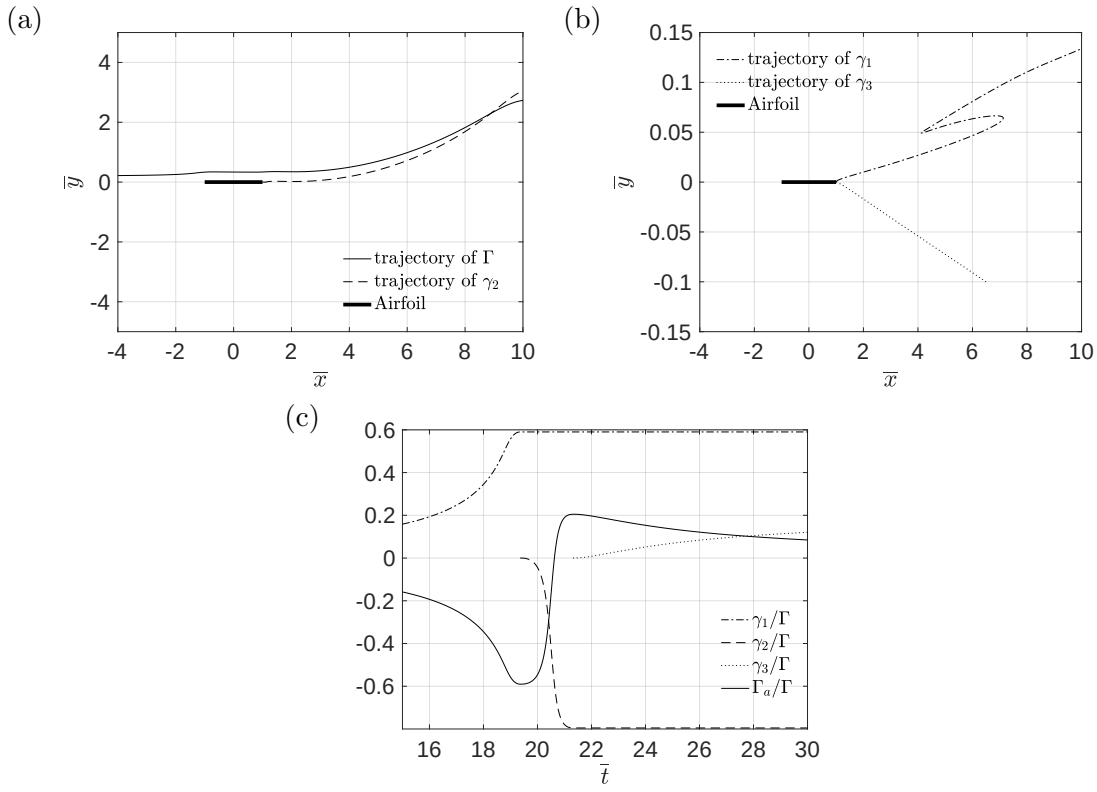

Figure 5.2: Trajectories of an incident line vortex Γ and three shed vortices γ_1, γ_2 and γ_3 from a flat plate airfoil in uniform flow with $\alpha = 0$: (a) trajectories of incident vortex Γ and trailing edge vortex γ_2; (b) trajectories of trailing edge vortices γ_1 and γ_3; (c) circulation of the connnected airfoil and trailing edge vortices in time.

5.3 Joukowski airfoil

5.3.1 Stationary airfoil

In this part, we compared the results with different airfoil thickness of a stationary Joukowski airfoil ($\varepsilon = 0$, $\alpha = 0^\circ$). First, we compared the trajectories of the incident vortex and three shedding vortices are composed in the cases of different airfoil thickness (0%, 15%, 25%, 35%), see Fig. 5.3. Since for 0% thickness is a degenerate case of the Joukowski airfoil and is also the same setup the multiple vortices shedding problem studied by Manela [14], a similar non-dimensional method and initial conditions are applied here: $\overline{x} = x/(2\lambda)$, $\overline{y} = y/(2\lambda)$ and $\overline{\Gamma} = \Gamma/(4\pi U\lambda)$, and the initial line vortex location is $\overline{z}_\Gamma(0) = z_\Gamma(0)/(2\lambda) = (-20, 0.2)$. The initial shed vortex location to be $\overline{z}_\gamma(0) = z_\gamma(0)/(2\lambda) = (1, 0.0001)$. The circulation of shedding vortices as well as the loads on the airfoil are compared in Fig. 5.4.

Figure 5.3 compares the trajectories of incident vortex Γ and shed vortices γ_1 and γ_2 and γ_3 for increasing values of airfoil thickness. The trajectories of γ_2, γ_3 and Γ have a similar shape for different values of airfoil thickness, where greater deviations are observed at long times for the thickest airfoil. However, the trajectory of γ_1 shows a sudden drop between the time range $12 < \bar{t} < 16$ when the airfoil thickness is 35%. Figure 5.4 shows that both the circulation of the shed vortices and of the airfoil change modestly but monotonically with airfoil thickness. As the airfoil thickness increases, the circulation of free vortices also increases (see Figs. 5.4 (a) and (b)).

The effects of different airfoil camber (0%, 4%, 9%) are also considered at fixed airfoil thickness (12%), and the airfoil camber reference NACA 4 digit airfoil calculation. Figure 5.5 compares the trajectories of incident vortex Γ and shed vortices γ_1 and γ_2 and γ_3 for increasing values of airfoil camber. The trajectories of γ_2, γ_3 and Γ have a similar shape for different values of airfoil camber, where greater deviation are observed at long times for the airfoil with largest camber. However, the trajectory of γ_1 shows a sudden drop between the time range $12 < \bar{t} < 15$ when the airfoil camber is 9%. Figure 5.6 shows that both the circulation of the shed vortices and of the airfoil change as models but monotonically with

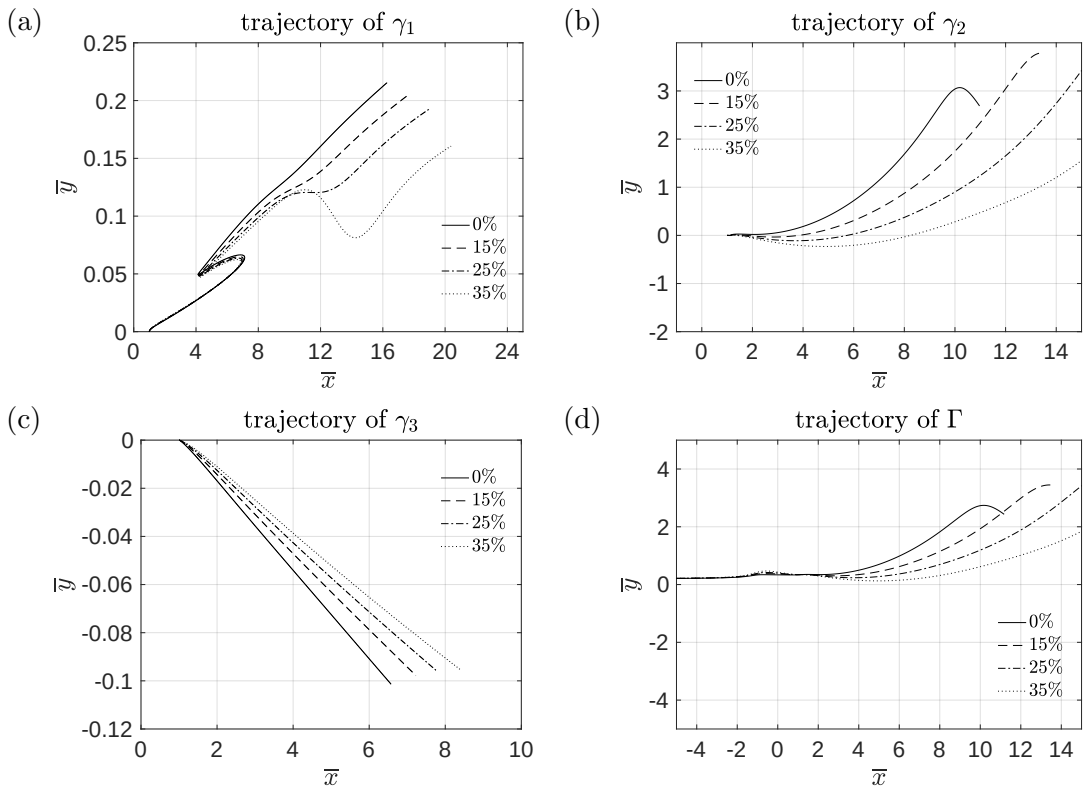

Figure 5.3: Trajectories of an incident line vortex Γ and three shed vortices γ_1, γ_2 and γ_3 from a stationary Joukowski airfoil with different thicknesses in uniform flow with $\alpha = 0$: (a) trajectories of trailing edge vortex γ_1; (b) trajectories of trailing edge vortex γ_2; (c) trajectories of trailing edge vortex γ_3; (d) trajectories of incident vortex Γ.

airfoil camber. As the airfoil camber increases, the circulation of free vortices also increases (see Figs. 5.6 (a) and (b)).

5.3.2 Harmonic airfoil motion

For a Joukowski airfoil that is not stationary ($\varepsilon \neq 0$, $\alpha = 0$), numerical-results are first compared against time variation of scaled airfoil circulation in Manela's paper [14] when $\varepsilon = 0.01$. The non-dimensional method and the initial conditions are similar to Manela, which are: $\overline{x} = x/(2\lambda)$, $\overline{y} = y/(2\lambda)$, $\overline{\omega} = (2\omega\lambda)/U$ and $\overline{\Gamma} = \Gamma/(4\pi U\lambda)$, and the initial line vortex location is $\overline{z_\Gamma}(0) = z_\Gamma(0)/(2\lambda) = (-20, 0.2)$. Setting the initial shed vortex location to be $\overline{z}_\gamma(0) = z_\gamma(0)/(2\lambda) = (1, 0.0001)$ and the heaving frequency $\overline{\omega} = 1$ and $\overline{\omega}$

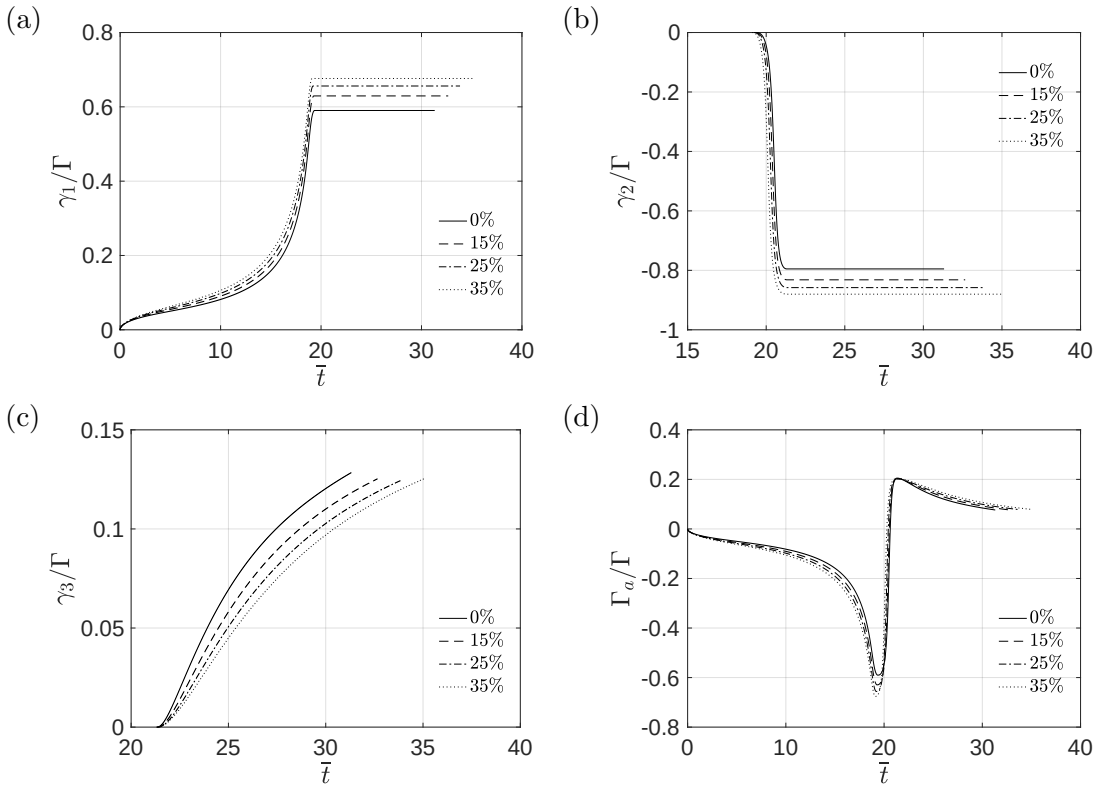

Figure 5.4: Strengths of the bound vorticity Γ_a/Γ and of the shed trailing edge vortices γ_n/Γ for a stationary Joukowski airfoil with different thicknesses in uniform flow with $\alpha = 0$: (a) circulation of trailing edge vortex γ_1; (b) circulation of trailing edge vortex γ_2; (c) circulation of trailing edge vortex γ_3; (d) circulation of incident vortex Γ.

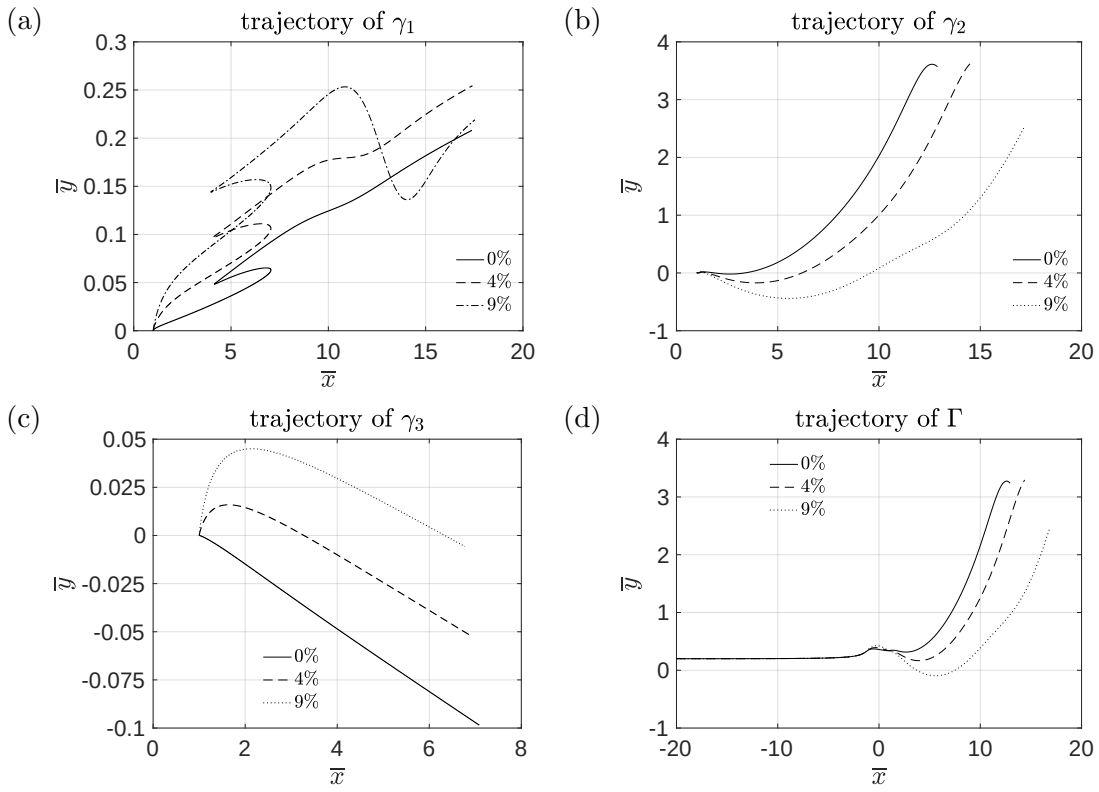

Figure 5.5: Trajectories of the incident vortex Γ and the shed trailing edge vortices γ_1, γ_2 and γ_3 for a stationary Joukowski airfoil (NACA 4 digit airfoil) with different camber in uniform flow with $\alpha = 0$: (a) trajectories of trailing edge vortex γ_1; (b) trajectories of trailing edge vortex γ_2; (c) trajectories of trailing edge vortex γ_3; (d) trajectories of incident vortex Γ.

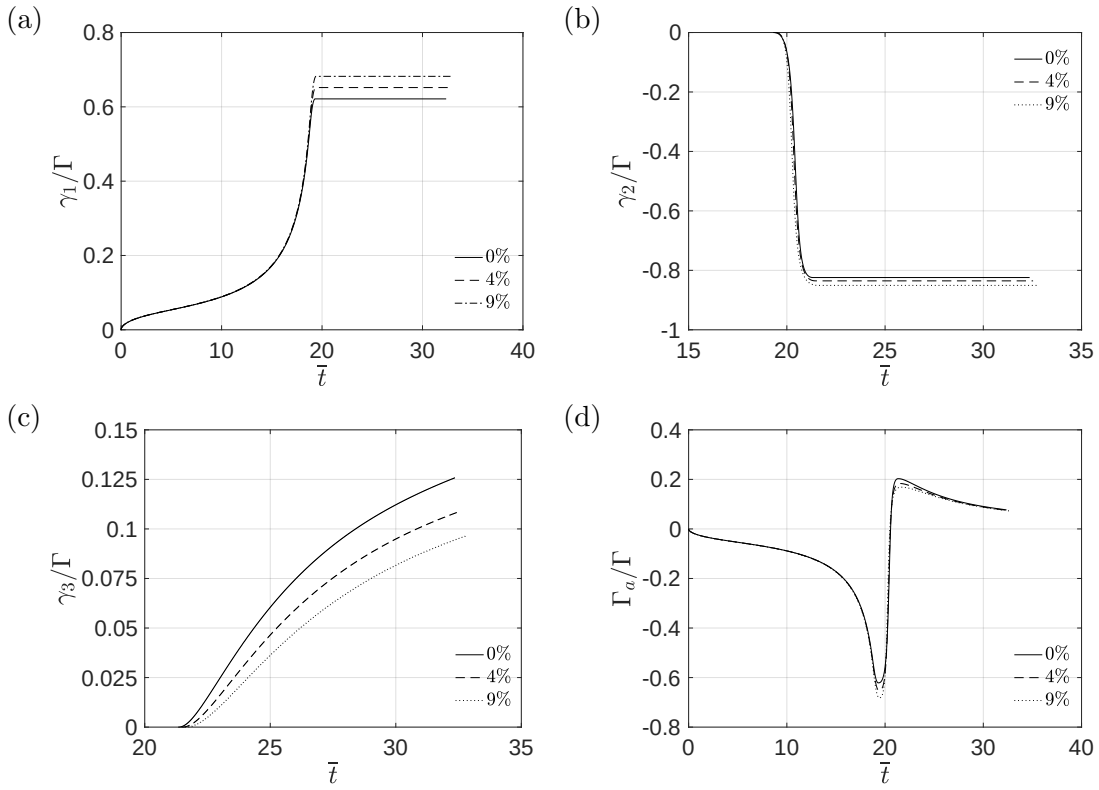

Figure 5.6: Strengths of the bound vorticity Γ_a/Γ and of the shed trailing edge vortices γ_n/Γ for a stationary Joukowski airfoil (NACA 4 digit airfoil) with different camber in uniform flow with $\alpha = 0$: (a) circulation of trailing edge vortex γ_1; (b) circulation of trailing edge vortex γ_2; (c) circulation of trailing edge vortex γ_3; (d) circulation of incident vortex Γ.

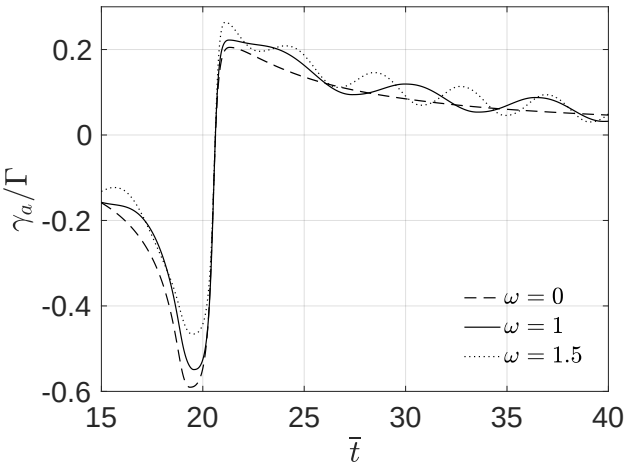

Figure 5.7: Time variation of scaled bound circulation for different frequencies of airfoil plunging oscillation

= 1.5, respectively. The results are shown in Figure 5.7, which agree with Fig. 4.(d) in Manela [14].

The influence of different airfoil thickness (0%, 15%, 25%, 35%) are now explained for prescribed heaving motions at fixed frequency, $\overline{\omega} = 1$. The result of time-varying scaled bound circulation is presented in Fig. 5.8, which shows that there is a dramatic change of the bound circulation near $\bar{t} \approx 20$ for all airfoil thicknesses. The considered reason may be because when the incident vortex approaches the airfoil, the unsteady interaction between the vortex and the airfoil becomes stronger and results in a large change in bound circulation. Specifically, as airfoil thickness increases, the bound circulation deviates more when the incident vortex is approaching the airfoil. After the incident vortex passes by the airfoil, the interactions between the fluid and airfoil weaken, and the bound circulation decreases to zero at large times as expected. Figure 5.8 also shows that with increasing of airfoil thickness, the attenuation of bound circulation (damping) becomes weaker after the time when the incident vortex passing by the airfoil. The effect of different airfoil camber is also studied, for a Joukowski airfoil with 12% thickness, consider different airfoil camber (0%, 4%, 9%) for the same frequency of prescribed heaving motion ($\overline{\omega} = 1$). The result of time-varying scaled bound circulation is presented in Fig. 5.9, which shows that the bound

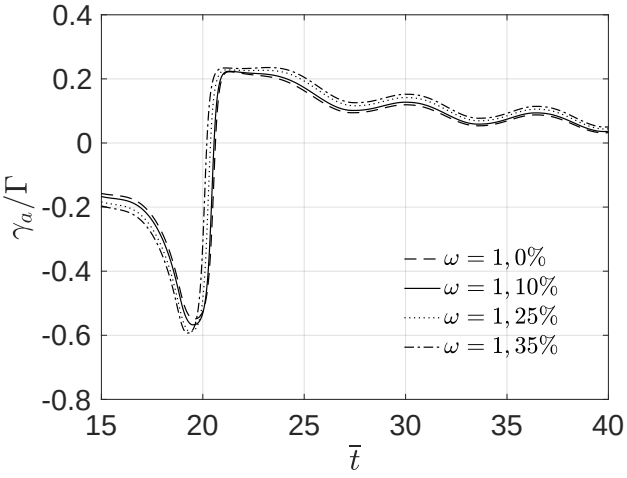

Figure 5.8: Time variation of scaled bound circulation for different airfoil thickness under the same frequency of airfoil plunging oscillation, $\overline{\omega} = 1$.

circulation has a similar shape for different values of airfoil camber, where smaller deviations are observed even at longer times.

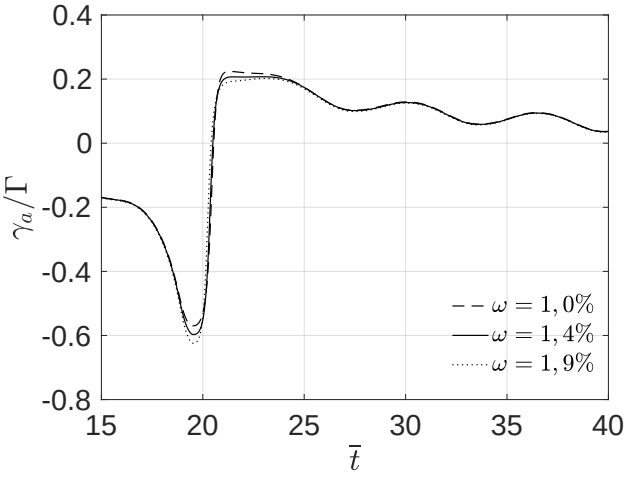

Figure 5.9: Time variation of scaled bound circulation for different airfoil camber with same airfoil thickness (12%) and under the same frequency of airfoil plunging oscillation, $\overline{\omega} = 1$.

Chapter 6

Conclusions and Future Directions

This work studies the effects of the geometry and harmonic motions of Joukowski airfoil in gust-airfoil interactions upon the evolution of trailing edge wake. A review of the current literature and existing theory that models the trailing edge wake. This thesis compares with existing theory as well as with previous work of Manela [14] for validation, and the comparison is divided into two parts: (1) starting vortex problem; (2) multiple shed vortices problem. Verification of (1) agrees with the starting vortex theory, and the comparison of (2) agrees with the results found by Manela.

Upon the above comparisons, a set of modifications are made that make it possible to study the interactions between unsteady gust and a Joukowski airfoil with different geometry. The modifications are divided into two main research investigations: (1) the stationary Joukowski airfoil with different geometry (camber and thickness); (2) the Joukowski airfoil with different geometry (camber and thickness) under prescribed harmonic motion with different frequencies. However, both model problems are restricted to a uniform flow under zero airfoil angle of attack, and the formulation of pertinent mathematical models will be modified if a non-zero angle of attack is considered. Results of (1) show that there are always three vortices shed from the trailing edge from a stationary Joukowski airfoil with various airfoil thickness or camber, and both the trajectories and the strengths of vortices change modestly but monotonically with airfoil thickness or camber, except for the tra-

jectory of the first shed vortex when the airfoil thickness or the camber is at maximum, which shows greater deviation in its trajectories in long times. Results of (2) agree with Manela [14] when different frequencies of oscillation for a flat plate airfoil are considered, and the results also shows that the bound circulation of a Joukowski airfoil under same frequency of oscillation changes modestly with airfoil thickness or camber.

6.1 Future Work

Future work on this topic will include analyses that may be organized into three different research investigations. First, the effects of elastic supports for a Joukowski airfoil on the aeroelastic coupling between the incident vortex and airfoil may be considered. Second, the plunging motion of a Joukowski airfoil at a non-zero angle of attack may also be developed as an extension of the present work. Lastly, the two future investigations could inform the prediction of vortex sound due to the vortex-airfoil interactions.

Appendix A

Scalar form of emended Brown and Michael equation

The original emended Brown and Michael equation is [8]

$$\frac{d\boldsymbol{x}_{\gamma_n}}{dt} \cdot \boldsymbol{\nabla}\Psi_i + \frac{\Psi_i}{\gamma_n}\frac{d\gamma_n}{dt} = \boldsymbol{v}_{\gamma_n} \cdot \boldsymbol{\nabla}\Psi_i, \qquad i = 1, 2 \tag{A.1}$$

(A.1) can be expanded in vector formats as

$$\left(\frac{dx}{dt}, \frac{dy}{dt}\right) \cdot \left(\frac{\partial\Psi_1}{\partial x}, \frac{\partial\Psi_1}{\partial y}\right) + \frac{\Psi_1}{\gamma_n}\frac{d\gamma_n}{dt} = (v_x, v_y) \cdot \left(\frac{\partial\Psi_1}{\partial x}, \frac{\partial\Psi_1}{\partial y}\right), \tag{A.2}$$

$$\left(\frac{dx}{dt}, \frac{dy}{dt}\right) \cdot \left(\frac{\partial\Psi_2}{\partial x}, \frac{\partial\Psi_2}{\partial y}\right) + \frac{\Psi_2}{\gamma_n}\frac{d\gamma_n}{dt} = (v_x, v_y) \cdot \left(\frac{\partial\Psi_2}{\partial x}, \frac{\partial\Psi_2}{\partial y}\right). \tag{A.3}$$

(A.2) and (A.3) can be also expanded respectively as

$$\frac{dx}{dt}\frac{\partial\Psi_1}{\partial x} + \frac{dy}{dt}\frac{\partial\Psi_1}{\partial y} + \frac{\Psi_1}{\gamma_n}\frac{d\gamma_n}{dt} = v_x\frac{\partial\Psi_1}{\partial x} + v_y\frac{\partial\Psi_1}{\partial y}, \tag{A.4}$$

$$\frac{dx}{dt}\frac{\partial\Psi_2}{\partial x} + \frac{dy}{dt}\frac{\partial\Psi_2}{\partial y} + \frac{\Psi_2}{\gamma_n}\frac{d\gamma_n}{dt} = v_x\frac{\partial\Psi_2}{\partial x} + v_y\frac{\partial\Psi_2}{\partial y}. \tag{A.5}$$

From (A.4) and (A.5), the general scalar form of emended Brown and Michael equation

may be written as

$$\frac{dx}{dt} + \frac{\Psi_1 \frac{\partial \Psi_2}{\partial y} - \Psi_2 \frac{\partial \Psi_1}{\partial y}}{\frac{\partial \Psi_1}{\partial x}\frac{\partial \Psi_2}{\partial y} - \frac{\partial \Psi_2}{\partial x}\frac{\partial \Psi_1}{\partial y}} \frac{1}{\gamma_n}\frac{d\gamma_n}{dt} = v_x, \tag{A.6}$$

$$\frac{dy}{dt} + \frac{\Psi_1 \frac{\partial \Psi_2}{\partial x} - \Psi_2 \frac{\partial \Psi_1}{\partial y}}{\frac{\partial \Psi_1}{\partial y}\frac{\partial \Psi_2}{\partial x} - \frac{\partial \Psi_2}{\partial y}\frac{\partial \Psi_1}{\partial x}} \frac{1}{\gamma_n}\frac{d\gamma_n}{dt} = v_y. \tag{A.7}$$

Let

$$H_1 = \frac{\Psi_1 \frac{\partial \Psi_2}{\partial y} - \Psi_2 \frac{\partial \Psi_1}{\partial y}}{\frac{\partial \Psi_1}{\partial x}\frac{\partial \Psi_2}{\partial y} - \frac{\partial \Psi_2}{\partial x}\frac{\partial \Psi_1}{\partial y}}, \tag{A.8}$$

$$H_2 = \frac{\Psi_1 \frac{\partial \Psi_2}{\partial x} - \Psi_2 \frac{\partial \Psi_1}{\partial y}}{\frac{\partial \Psi_1}{\partial y}\frac{\partial \Psi_2}{\partial x} - \frac{\partial \Psi_2}{\partial y}\frac{\partial \Psi_1}{\partial x}}. \tag{A.9}$$

Expressions (A.6) and (A.7) can be rearranged into

$$\frac{dz^*_{\gamma_n}}{dt} + (H_1 - iH_2)\frac{1}{\gamma_n}\frac{d\gamma_n}{dt} = v^*_{\gamma_n}, \tag{A.10}$$

where $z^*_{\gamma_n} = x - iy$, and $v^*_{\gamma_n} = v_x - iv_y$.

Equation (A.8) can be regarded as a general scalar form of the emended Brown and Michael equation for future theoretical analyses. Once the stream function Ψ_i $(i = 1, 2)$ is known, it is possible to get $\boldsymbol{\nabla}\Psi_i = (\partial\Psi_i/\partial x, \partial\Psi_i/\partial y)$, thus H_1 and H_2 are known, and the vortex motion can be analyzed from (A.8).

Appendix B

Emended Brown and Michael equation for multiple shed vortices

The original emended Brown and Michael equation in [8]:

$$\frac{d\boldsymbol{x}_{\gamma_n}}{dt} \cdot \boldsymbol{\nabla}\Psi_i + \frac{\Psi_i}{\gamma_n}\frac{d\gamma_n}{dt} = \boldsymbol{v}_{\gamma_n} \cdot \boldsymbol{\nabla}\Psi_i, \qquad i = 1, 2 \tag{B.1}$$

(B.1) can be expanded in vector formats as

$$\left(\frac{dx}{dt}, \frac{dy}{dt}\right) \cdot \left(\frac{\partial\Psi_1}{\partial x}, \frac{\partial\Psi_1}{\partial y}\right) + \frac{\Psi_1}{\gamma_n}\frac{d\gamma_n}{dt} = (v_x, v_y) \cdot \left(\frac{\partial\Psi_1}{\partial x}, \frac{\partial\Psi_1}{\partial y}\right), \tag{B.2}$$

$$\left(\frac{dx}{dt}, \frac{dy}{dt}\right) \cdot \left(\frac{\partial\Psi_2}{\partial x}, \frac{\partial\Psi_2}{\partial y}\right) + \frac{\Psi_2}{\gamma_n}\frac{d\gamma_n}{dt} = (v_x, v_y) \cdot \left(\frac{\partial\Psi_2}{\partial x}, \frac{\partial\Psi_2}{\partial y}\right). \tag{B.3}$$

(B.2) and (B.3) can be also expanded respectively as

$$\frac{dx}{dt}\frac{\partial\Psi_1}{\partial x} + \frac{dy}{dt}\frac{\partial\Psi_1}{\partial y} + \frac{\Psi_1}{\gamma_n}\frac{d\gamma_n}{dt} = v_x\frac{\partial\Psi_1}{\partial x} + v_y\frac{\partial\Psi_1}{\partial y}, \tag{B.4}$$

$$\frac{dx}{dt}\frac{\partial\Psi_2}{\partial x} + \frac{dy}{dt}\frac{\partial\Psi_2}{\partial y} + \frac{\Psi_2}{\gamma_n}\frac{d\gamma_n}{dt} = v_x\frac{\partial\Psi_2}{\partial x} + v_y\frac{\partial\Psi_2}{\partial y}. \tag{B.5}$$

The stream function of the flat plate airfoil is [11]

$$\Psi_1 = \mathrm{Im}\{z\} \quad \text{and} \quad \Psi_2 = \mathrm{Im}\left\{-i\sqrt{z^2 - a^2}\right\}, \tag{B.6}$$

can be rearranged in the following manner:

$$\begin{aligned}
\boldsymbol{\nabla}\Psi_1 &= \boldsymbol{\nabla}\mathrm{Im}\{z\} = \mathrm{Im}\{\boldsymbol{\nabla}z\}, \\
&= \mathrm{Im}\{\boldsymbol{\nabla}(x+iy)\}, \\
&= \mathrm{Im}\{(1,i)\}, \\
&= (0,1) = \left(\frac{\partial\Psi_1}{\partial x}, \frac{\partial\Psi_1}{\partial y}\right). \qquad \text{(B.7)}
\end{aligned}$$

Also

$$\begin{aligned}
\boldsymbol{\nabla}\Psi_2 &= \mathrm{Im}\left\{\boldsymbol{\nabla}\left(-i\sqrt{z^2-a^2}\right)\right\}, \\
&= \mathrm{Im}\left\{\boldsymbol{\nabla}(z)\frac{d\left(-i\sqrt{z^2-a^2}\right)}{dz}\right\}, \\
&= \mathrm{Im}\left\{(1,i)\left(-i\frac{z}{\sqrt{z^2-a^2}}\right)\right\}, \\
&= \mathrm{Im}\left\{\left(-i\frac{z}{\sqrt{z^2-a^2}}, \frac{z}{\sqrt{z^2-a^2}}\right)\right\} = \left(\frac{\partial\Psi_2}{\partial x}, \frac{\partial\Psi_2}{\partial y}\right). \qquad \text{(B.8)}
\end{aligned}$$

Substituting (B.7) into (B.4) yields

$$\frac{dy}{dt} + \frac{y}{\gamma_n}\frac{d\gamma_n}{dt} = v_y. \qquad \text{(B.9)}$$

Then substitution of (B.8) into (B.5) produces

$$\frac{dx}{dt} + \frac{\Psi_2 - y\frac{\partial\Psi_2}{\partial y}}{\frac{\partial\Psi_2}{\partial x}}\frac{1}{\gamma_n}\frac{d\gamma_n}{dt} = v_x. \qquad \text{(B.10)}$$

Combine (B.7), (B.8), (B.9) and (B.10) to get the complex equation of motion

$$\frac{dz^*_{\gamma_n}}{dt} + \left(\frac{\mathrm{Im}\left\{-i\sqrt{z^2_{\gamma_n}-a^2}\right\} - y\mathrm{Im}\left\{\frac{z_{\gamma_n}}{\sqrt{z^2_{\gamma_n}-a^2}}\right\}}{\mathrm{Im}\left\{-i\frac{z_{\gamma_n}}{\sqrt{z^2_{\gamma_n}-a^2}}\right\}} - iy\right)\frac{1}{\gamma_n}\frac{d\gamma_n}{dt} = v^*_{\gamma_n}, \qquad \text{(B.11)}$$

which is equivalent to (A.10) derived by alternate means.

Biography

Huansheng Chen earned his undergraduate degree in aerospace engineering from BEIHANG University in China and is currently a M.S. student in Mechanical Engineering and Mechanics at Lehigh University. His research interests include computational fluid dynamics modeling and fluid-structure interactions.

Bibliography

[1] G. K. Batchelor. *An Introduction to Fluid Dynamics*. Cambridge University Press, United Kingdom, United Kingdom, 1967.

[2] R. L. Bisplinghoff, H. Ashley, and R. L. Halfman. *Aeroelasticity*. 1st ed. Dover Publications, Inc., New York, 1996.

[3] C. E. Brown. "Effect of leading-edge separation on the lift of a delta wing". *Journal of the Aeronautical Sciences* 21.10 (1954), pp. 690–694.

[4] L. Cortelezzi and A. Leonard. "Point vortex model of the unsteady separated flow past a semi-infinite plate with transverse motion". *Fluid Dynamics Research* 11.6 (1993), p. 263.

[5] *Geese fly in a "V" formation*. URL: `https://assets3.thrillist.com/v1/image/2403832/size/sk-2017_04_article_main_desktop_2x.jpg`.

[6] Y. P. Guo. "Application of the Ffowcs Williams/Hawkings equation to two-dimensional problems". *Journal of Fluid Mechanics* 403 (2000), pp. 201–221.

[7] M. S. Howe. *Acoustics and aerodynamic sound*. Cambridge University Press, United Kingdom, 2014.

[8] M. S. Howe. "Emendation of the Brown & Michael equation, with application to sound generation by vortex motion near a half-plane". *Journal of Fluid Mechanics* 329 (1996), pp. 89–101.

[9] M. S. Howe. *Hydrodynamics and sound*. Cambridge University Press, United Kingdom, 2006.

[10] M. S. Howe. "Influence of separation on sound generated by vortex-step interaction". *Journal of fluids and structures* 11.8 (1997), pp. 857–872.

[11] M. S. Howe. *Theory of vortex sound*. Vol. 33. Cambridge University Press, United Kingdom, 2003.

[12] A. M. Kuethe and C. Y. Chow. *Foundations of Aerodynamics: Bases of Aerodynamic Design, 1998*. John Wiley & Sons, Inc., New York, NY.

[13] C.-Y. Kuo and A. P. Dowling. "Acoustics of a two-dimensional compact jet impinging normally onto a flat plate". *Journal of Fluid Mechanics* 414 (2000), pp. 251–284.

[14] A. Manela. "Nonlinear effects of flow unsteadiness on the acoustic radiation of a heaving airfoil". *Journal of Sound and Vibration* 332.26 (2013), pp. 7076–7088.

[15] A. Manela and L. Huang. "Point vortex model for prediction of sound generated by a wing with flap interacting with a passing vortex". *The Journal of the Acoustical Society of America* 133.4 (2013), pp. 1934–1944.

[16] S. Michelin and S. G. Llewellyn Smith. "Resonance and propulsion performance of a heaving flexible wing". *Physics of Fluids* 21.7 (2009), p. 071902.

[17] S. Michelin, S. G. Llewellyn Smith, and B. J. Glover. "Vortex shedding model of a flapping flag". *Journal of Fluid Mechanics* 617 (2008), pp. 1–10.

[18] M. C. A. M. Peters and A. Hirschberg. "Acoustically induced periodic vortex shedding at sharp edged open channel ends: simple vortex models". *Journal of Sound and Vibration* 161.2 (1993), pp. 281–299.

[19] D. O. Rockwell. "Vortex-body interactions". *Annual Review of Fluid Mechanics* 30.1 (1998), pp. 199–229.

[20] C. Thomas. *F/A-18 Autonomous Formation Flight (AFF)*. URL: `https://www.nasa.gov/centers/dryden/multimedia/imagegallery/AFF/EC01-0328-3.html`.

[21] C. J. Wang and J. D. Eldredge. "Low-order phenomenological modeling of leading-edge vortex formation". *Theoretical and Computational Fluid Dynamics* 27.5 (2013), pp. 577–598.